Intense Monochromatic Photons Above 100 keV From An Inverse Compton Source at the Cornell-BNL ERL Test Accelerator

Kirsten Deitrick, Carl Franck, and Georg Hoffstaetter
Cornell University, USA

Bruno D. Muratori and Peter Williams
STFC Daresbury Laboratory and Cockcroft Institute, UK

Geoff Krafft and Balša Terzić
Old Dominion University and Thomas Jefferson National Accelerator Facility, USA

Joe Crone and Hywel Owen
The University of Manchester and Cockcroft Institute, UK
(Dated: September 8, 2020)

Quasi-monochromatic x-rays are difficult to produce above 100 keV, but have a number of uses in x-ray and nuclear science, particularly in the analysis of transuranic species. We study Inverse Compton scattering (ICS) of a recirculated 1064 nm laser with $a_0 \ll 1$ to hard x-ray photons using modest electron energies. Here we predict the expected ICS flux from operating the 42–150 MeV CBETA multi-turn energy-recovery linac using an incident laser repetition rates of 162.5 MHz. Collimated fluxes within a 0.5% bandwidth greater than 10^8 photons per second are expected using demonstrated CBETA bunch properties, with scattered photon energies extending beyond 400 keV for electron energies of 150 MeV. At these high energies ICS flux exceeds that attainable from storage ring sources of synchrotron radiation, even though CBETA is a compact accelerator system. We foresee that future energy-recovery linacs may generate MeV photon energies from Compton scattering with properties unattainable using other methods, enabling wide applications in nuclear science.

I. INTRODUCTION

Intense sources of high-energy photons above 1 keV can be obtained in the laboratory in one of four practical ways: discrete line gamma sources from radioactive decay, bremsstrahlung of electrons within a solid target, synchrotron radiation (SR), and inverse Compton scattering (ICS). Such sources are today the mainstay of many areas of scientific study. Storage ring production of narrowband undulator x-rays from 1 to 100 keV (which requires GeV-scale electrons) has very broad use across many topics including diffraction and spectroscopy; broadband bremsstrahlung from lower-energy electrons (typically tens of MeV) finds application in imaging and nuclear physics, particularly when applied to the identification and quantification of nuclear materials using MeV-scale photons. Bremmsstrahlung sources are technically convenient but not ideal due to their inherent large photon energy spread.

Important techniques using high-energy photons are x-ray absorption spectroscopy (XAS), x-ray fluorescence (XRF), and nuclear resonance fluorescence (NRF); for samples with high atomic number Z these have numerous applications in nuclear physics, industry, and nuclear security. For example, a high-Z nucleus such as uranium ($Z = 92$) has Kα_2 and Kα_1 energies of 94.7 keV and 98.4 keV respectively (K edge energy 115.6 keV) – photons of higher energies are needed to probe transuranic species. Similarly, NRF can be used to discriminate with precision the quantities of transuranic isotopes in large samples (such as spent nuclear fuel canisters) using photons in the 1 to 3 MeV range (for example, ^{235}U detection needs 1.733 MeV photons) [1].

Bremsstrahlung sources generate a large quantity of unused photons at lower energies that may cause a number of instrumental issues; ideally, a monochromatic (or quasi-monochromatic) source is desired. Electron storage rings at the higher practicable stored bunch energies around 6-8 GeV (such as the national facilities ESRF, APS, and SPRING-8) can generate intense, monochromatic photons up to ∼100 keV in the first harmonic of their undulators. However, these sources are hardly compact (the storage rings are around 1 km in circumference), and their output does not readily extend to the MeV scale.

ICS in the head-on geometry using the common 1064 nm incident wavelength (photon energy $E_{\text{laser}} = 1.17$ eV) gives backscattered photons of energy

$$E_\gamma = 4\gamma^2 E_{\text{laser}} \tag{1}$$

for electrons with Lorentz factor $\gamma = E_e/m_e c^2$. Hence, electrons with energy $E_e \simeq 75$ MeV are needed to produce 100 keV photons, and $E_e \simeq 240$ MeV is needed for 1 MeV photons. With sufficient scattering rate and suitable collimation, ICS sources using moderate electron energy may generate intense MeV-scale photons.

Here we describe the advantages offered by an energy recovery linac (ERL) driven ICS light source as an intense source of MeV-scale photons, and provide an example of such a source based on the recently-

commissioned multi-turn ERL utilizing superconducting radio-frequency (SRF) cavities: CBETA - the Cornell-BNL ERL Test Accelerator [2]. We show below that the demonstrated bunch parameters can provide a flux of monochromatic x-rays that can extend up to 400 keV, providing a flux not readily attainable in other ways. We then discuss how a modest extension of these existing parameters allows generation of intense fluxes of photons into the MeV regime. We will argue that ERLs offer a realistic route to generating MeV photons, where they may combine the energy-efficient aspects of energy recovery of the drive beam with the use of permanent-magnet beam transport.

II. THE CBETA ACCELERATOR

A. Motivation for an Energy-Recovery Linac

In the early days of high energy accelerators, two main categories existed: linear and circular; today, linacs and storage rings are both commonplace. As a generalization, electron linacs are typically capable of producing higher-quality beams (e.g. smaller emittance and bunch length) than storage rings. However, this comes with a lower energy efficiency than a storage ring; storage rings commonly produce average currents > 10 mA that would be impossible in a linac – the radio-frequency (RF) power cost and beam dump losses would be prohibitive.

ERLs combine the best of both types of accelerators; they can typically deliver higher-quality beams than those in storage rings, with greater energy efficiency than a linac [3]. In a typical one-turn ERL, a low energy beam is injected into a string of SRF cavities which accelerate the beam; the beam is then transported back to the cavity string where it is decelerated before being transported to a beam stop. The electrons' kinetic energy is returned to the RF field of the cavities and is used to accelerate following bunches; this allows for the beam power in the ERL to greatly exceed the available RF power. As the beam parameters necessary for scientific research call for higher current and higher quality beams, ERLs are the accelerators best-suited to meet this demand. Multi-turn ERLs, which accelerate the electron beam multiple times before decelerating the beam, have the benefit of being able to reach higher energies without additional cost, power requirements, or floor space [4]. The multi-turn layout of the CBETA accelerator considered here is shown in Fig. 1.

B. The Cornell-BNL ERL Test Accelerator

CBETA – the Cornell-BNL ERL Test Accelerator – is the first successful demonstration of an SRF multi-turn ERL [2, 5]; it features a non-scaling Fixed-Field Alternating-gradient (FFA) arc constructed using permanent (Halbach-type) combined-function magnets, which

Parameter	Quantity	Units
Kinetic energy	42, 78, 114, and 150	MeV
RF frequency	1.3	GHz
Bunch charge	≤ 2	nC
Repetition rate	$1.3/N$ (integer N)	GHz
Maximum current	100 (one-turn), 40 (four-turn)	mA

TABLE I: Key design parameters of CBETA.

transport the four beam energies (42, 78, 114, and 150 MeV) simultaneously in a common transport beam pipe. CBETA is principally aimed at demonstrating the ERL technologies needed for a future electron-ion collider [5], but its parameters are also very attractive when considering hard x-ray photon production via ICS. CBETA comprises a 6 MeV injector, a single main linac cryomodule (MLC), splitter/recombiner sections (SX and RX), FFA arc (FA, TA, ZX, TB, FB), and beam stop; the layout of the four-turn configuration is shown in Fig. 1.

CBETA may be configured to operate using from one to four turns, with the corresponding top energies of each configuration being 42, 78, 114, and 150 MeV respectively; the design parameters are given in Table I. For a configuration of Y turns, the beam completes $2Y$ passes through the MLC, and $2Y-1$ passes through the FFA arc. The FFA arc can be divided into five sections: the arc sections (FA, FB) consist of FFA arc cells; the straight section (ZX) consists of FFA straight cells; and the transition sections (TA, TB) serve to match the beam between the arc and straight sections.

In the SX and RX sections, each beam energy passes through a different splitter/recombiner; this gives control of the Twiss parameters, horizontal dispersion and its derivative, R_{56}, and orbit; path length is varied using moving stages. The SX/RX lines are numbered one to four (S1, S2, etc) corresponding to increasing beam energy, with the lowest-energy lines (S1/R1) on the inside and successive higher-energy lines further out. Each line simultaneously transports two beams – an accelerated pass and a decelerated pass – apart from at the highest-energy pass. Consequently, the beam optics of the accelerating and decelerating passes in the splitter lines are inherently coupled [5].

Four passes have recently been experimentally demonstrated, with details given in Bartnik et al. [2]; this confirms that an ERL may deliver the beam parameters discussed in this paper.

III. INVERSE COMPTON SCATTERING SOURCES

A. Inverse Compton Scattering Physics

Following their original description by Feenberg and Primakoff [6], sources based on inverse Compton scattering (ICS) – the process of scattering a photon from a
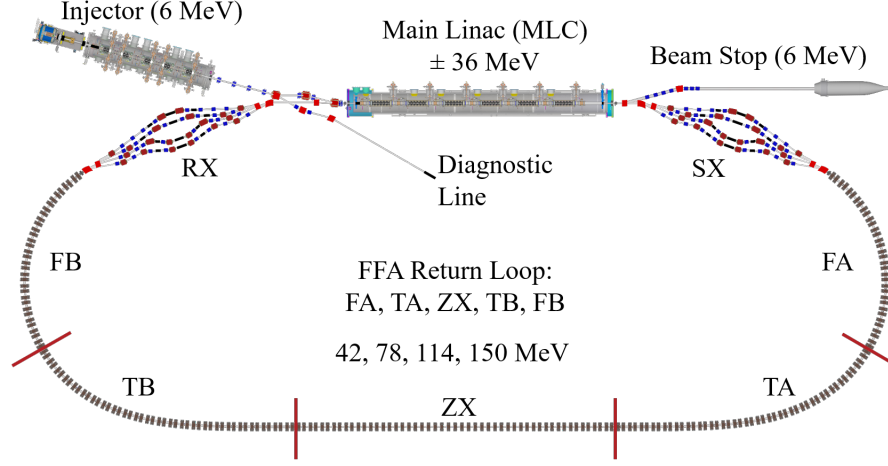
FIG. 1: Overview of the CBETA accelerator; a single FFA common transport arc (that includes the straight FFA section ZX) carries all four beam energies (42, 78, 114, and 150 MeV) within a single beam pipe. Matching of the entrance and exit beams at each energy is obtained through the SX and RX sections.

relativistic-moving electron – have emerged as a promising way to generate tuneable, monochromatic photons across output energies from tens of keV as far as the GeV scale [7–9]. The energy of the scattered photons – taking into account electron recoil – is given by

$$E_\gamma = \frac{E_{\text{laser}}\,(1 - \beta\cos\phi')}{1 - \beta\cos\theta + (1 - \cos\theta')E_{\text{laser}}/E_e} \qquad (2)$$

where $E_e = \gamma mc^2$ is the incident (total) electron energy, E_{laser} is the incident (laser) photon energy, $\beta = v/c$, θ the angle between the incident electrons and the outgoing scattered photons, and ϕ' the angle between the incident electrons and incident photons. $\theta' = \phi' - \theta$ is the angle between the incident and scattered photons and $\phi = \pi - \phi'$ is the crossing angle. The geometry of the interaction point (IP) and these angles are shown in Fig. 2 [10, 11].

The highest-energy photons are produced in a head-on collision between an electron and photon ($\phi' = \pi$), when photons are back-scattered into the same direction as the incident electron ($\theta = 0$); this highest photon energy is referred to as the Compton edge. Taking the electron recoil into account, the maximum energy of the scattered photons is given by

$$E_\gamma^{\text{max}} = \frac{4\gamma^2 E_{\text{laser}}}{1 + X}, \qquad (3)$$

where $X = 4\gamma E_{\text{laser}}/mc^2$ is the electron recoil parameter [12]. The Thomson regime is when electron recoil is negligible ($X \ll 1$), and the Compton edge energy[1]

───────

[1] the Compton edge corresponds to those photons which are backscattered
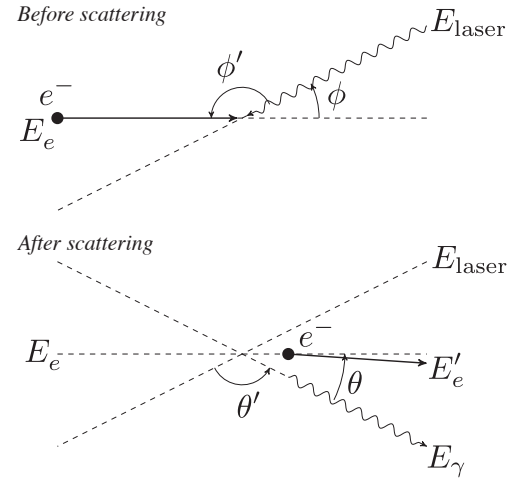

FIG. 2: Geometry of scattering at the inverse Compton Scattering interaction point; follows Fig. 1 from Sun et al. [11].

becomes

$$E_\gamma^{\text{max}} = 4\gamma^2 E_{\text{laser}}. \qquad (4)$$

In this regime, the scattering interaction can be viewed as an elastic collision. Electron recoil becomes significant when both γ and E_{laser} are large, and in this situation

$$E_\gamma \to E_e; \qquad (5)$$

the scattered photon energy cannot have more energy than the incident electron. A practical example of this is the proposed collision of 12 keV FEL photons with 7 GeV electrons within a storage ring ($X \sim 1000$),

where the scattered photon energy becomes essentially also 7 GeV [13].

Compton scattering can be treated as analogous to undulator radiation. In that vein, the undulator K-parameter is similar to the laser field strength parameter a_0 for Compton scattering, which is

$$a_0 = \frac{eE\lambda_{\text{laser}}}{2\pi mc^2}; \tag{6}$$

e is the electron charge, E the transverse electric field of the laser, and λ_{laser} is the wavelength of the incident photons. Here we assume the linear regime where $a_0 \ll 1$, and all later formulae assume that [10].

In a collision between an electron bunch (containing N_e electrons) and a laser pulse (containing N_{laser} photons), the total number of scattered photons N_γ for a crossing angle ϕ is given by [14]

$$N_\gamma = \sigma_c \frac{N_e N_{\text{laser}} \cos\left(\phi/2\right)}{2\pi\sigma_y\sqrt{\sigma_x^2\cos^2\left(\phi/2\right) + \sigma_z^2\sin^2\left(\phi/2\right)}} \tag{7}$$

where σ_c is the Compton scattering cross-section and $\sigma_i^2 = \sigma_{\text{electron},i}^2 + \sigma_{\text{laser},i}^2$ is the convoluted spot size of the electron and laser beam in each direction ($i = x, y, z$) at the interaction point (IP). We note that for the same overlap of electron and laser spot sizes, the number of Compton-scattered photons is independent of electron energy in the Thomson regime where $\sigma_T \simeq \sigma_c$. The exact Compton cross-section from QED [15] is

$$\sigma_c = \sigma_T \frac{3}{4X}\left[\left(1 - \frac{4}{X} - \frac{8}{X}\right)\log(1+X)\right.$$

$$\left. + \frac{1}{2} + \frac{8}{X} - \frac{1}{2(1+X)^2}\right] \tag{8}$$

which reduces to

$$\sigma_c \simeq \sigma_T(1-X) \tag{9}$$

for small values of X; $\sigma_T = 6.65 \times 10^{-29}$ m^2 is the Thomson cross section [16]. For $\lambda_{\text{laser}} = 1064$ nm and typical $\gamma \sim 10^3$ we have $X \sim 10^{-2}$, and thus $\sigma_c \simeq \sigma_T$ to the percent level. Assuming the incident laser is approximately a plane wave, the number of scattered photons within a 0.1% bandwidth at the Compton edge is $N_{0.1\%} \simeq 1.5 \times 10^{-3} N_\gamma$. Consequently, the rate of photons (flux) into this bandwidth is $\mathcal{F}_{0.1\%} \simeq 1.5 \times 10^{-3}\dot{N}_\gamma$; $\mathcal{F} = \dot{N}_\gamma = fN_\gamma$ for sources of repetition rate f [10]. $N_{0.1\%}$ is independent of electron energy (assuming N_γ stays the same) since both E_γ^{max} and relative bandwidth scale together as γ^2. In the non-diffraction-limited case, where the laser spot size at the IP is significantly larger than the electron beam spot size, the average brilliance of the scattered photons (given in conventional units, i.e. mm^{-2}mrad^{-2} s^{-1} per 0.1%bw) is

$$\mathcal{B}_{\text{avg}} \approx \frac{\mathcal{F}_{0.1\%}}{4\pi^2\epsilon^2} = \frac{\gamma^2\mathcal{F}_{0.1\%}}{4\pi^2\epsilon_N^2}; \tag{10}$$

here, ϵ is the transverse emittance of the electron beam at the IP and ϵ_N is the normalised transverse emittance, where we assume a round beam. For a more detailed explanation, refer to Deitrick et al. [17].

The peak brilliance of the source (for a zero crossing angle) is calculated via an analytical formula of Hartemann et al. [18],

$$\mathcal{B}_{\text{peak}} = 10^{-15}\frac{4\gamma^2}{\pi^2\epsilon_N^2}\frac{N_e N_L}{\Delta\tau}\frac{r_0^2}{\sigma_{\text{laser}}^2}\exp\left\{\frac{\chi - 1}{2\chi\Delta u_\perp^2}\left[2 + \frac{\delta\omega^2 + \delta\gamma^2\chi^2}{2\chi\left(\chi - 1\right)\Delta u_\perp^2}\right]\right\}$$

$$\times\left[1 - \Phi\left\{\frac{\chi - 1}{\sqrt{\delta\omega^2 + \delta\gamma^2\chi^2}}\left[1 + \frac{\delta\omega^2 + \delta\gamma^2\chi^2}{2\chi\left(\chi - 1\right)\Delta u_\perp^2}\right]\right\}\right]\mathbb{F}\left(\eta, \mu\right), \tag{11}$$

where r_0 is the classical electron radius, $\Delta u_\perp = \epsilon_N/\sigma_{\text{electron}}$ is the perpendicular velocity spread, σ_{electron} the spot size of the electron bunch at the IP (assuming it is circular), $\Delta\tau$ is the electron bunch duration, $\delta\omega$ is the relative frequency spread of the laser, and $\delta\gamma$ is the relative energy spread of the electron beam; the 10^{-15} factor arises as a unit conversion from SI to mm^{-2}mrad^{-2}s^{-1} per 0.1% bw. The normalised Doppler up-shifted fre-

quency, χ, is given by

$$\chi = \frac{\omega_x}{4\gamma^2\omega_0}, \tag{12}$$

where ω_x and ω_0 are the angular frequency of the scattered and incident radiation and $\Phi\left(x\right)$ is the error function

$$\Phi\left(x\right) = \frac{2}{\sqrt{\pi}}\int_0^x e^{-t^2}\mathrm{d}t. \tag{13}$$

The overlap function $\mathbb{F}(\eta,\mu)$ is given by

$$\mathbb{F}(\eta,\mu) = \frac{\eta e^{1/\eta^2}\left[1 - \Phi(1/\eta)\right] - \mu e^{1/\mu^2}\left[1 - \Phi(1/\mu)\right]}{\eta^2 - \mu^2},\tag{14}$$

where $\eta = c\Delta t/2\sqrt{2}\beta^*$ is the normalised inverse β-function, Δt is the laser pulse duration, β^* the (Twiss) β-function at the IP, and $\mu = c\Delta t/2\sqrt{2}z_R$ is the normalised inverse Rayleigh length for a Rayleigh length $z_R = \pi\sigma_{\text{laser}}^2/\lambda$. The spectral density of the scattered photons is

$$\mathcal{S} = \frac{\mathcal{F}}{E_\gamma^{\max}},\tag{15}$$

where $\mathcal{F} = fN_\gamma$ is the total (uncollimated) flux and E_γ^{max} is the Compton edge energy of the scattered photons (Eq. 2).

Using the bandwidth obtained from the scaling laws of N. Ranjan et al. [12], the bandwidth of the scattered radiation passing through a collimator can be expressed as

$$\frac{\Delta E_\gamma}{E_\gamma} = \sqrt{\left(\frac{\sigma_\theta}{E_\theta}\right)^2 + \left(\frac{\sigma_e}{E_e}\right)^2 + \left(\frac{\sigma_L}{E_L}\right)^2 + \left(\frac{\sigma_\epsilon}{E_\epsilon}\right)^2},\tag{16}$$

where

$$\frac{\sigma_\theta}{E_\theta} = \frac{1}{\sqrt{12}}\frac{\Psi^2}{1 + X + \Psi^2/2},\tag{17}$$

$$\frac{\sigma_e}{E_e} = \frac{2 + X}{1 + X + \Psi^2}\frac{\Delta E_e}{E_e},\tag{18}$$

$$\frac{\sigma_L}{E_L} = \frac{1 + \Psi^2}{1 + X + \Psi^2}\frac{\Delta E_{\text{laser}}}{E_{\text{laser}}},\tag{19}$$

$$\frac{\sigma_\epsilon}{E_\epsilon} = \frac{2\gamma\epsilon_N}{\beta^*}.\tag{20}$$

Here, $\Psi = \gamma\theta_{\text{col}}$ is called the acceptance angle, θ_{col} is the (physical) collimation angle, X is the electron recoil parameter, $\Delta E_e/E_e = \delta\gamma/2$ is the energy spread of the electron beam, $\Delta E_{\text{laser}}/E_{\text{laser}} = \delta\omega \simeq 6.57 \times 10^{-4}$ is the laser photon energy spread, β^* is the β-function at the IP, and ϵ_N is the normalised emittance of the electron beam at the IP.

This formula allows for the contributions to the bandwidth of the scattered radiation to be separated into individual contributions from collimation (Eq. 17), electron beam energy spread (Eq. 18), laser energy spread (Eq. 19), and electron beam emittance (Eq. 20). For example, taking a general case of a linac based ICS ($E_e = 100$ MeV, $\epsilon_N = 0.5$ mm mrad, $\Delta E_e/E_e = 5\times10^{-4}$, $\lambda = 1064$ nm, $\Delta E_L/E_L = 6.57 \times 10^{-4}$, $\beta^* = 0.1$ m, $\theta_{\text{col}} = 0.5$ mrad) we can calculate the bandwidth

$$\frac{\Delta E_x}{E_x} = \sqrt{(2.77 \times 10^{-3})^2 + (9.90 \times 10^{-4})^2 + (6.57 \times 10^{-4})^2 + (1.95 \times 10^{-3})^2} = 0.36\%.$$

The dominant terms are the collimation term (Eq. 17) and the emittance term (Eq. 20), through correct design small bandwidth ICS sources can be built by minimising these terms.

B. ICS Accelerator and Parameter Considerations

In designing an ICS source a number of trade-offs are necessary due to the conflicting demands of electron beam dynamics and other technical limitations. The incident laser will typically be obtained using a high-power optical cavity (cavity powers have been demonstrated in the 10-100 kW range [19]), which limits the repetition rate of the interaction below a few hundred MHz; as the cavity repetition rate increases the optical cavity path length must decrease, which amplifies the engineering challenges of the optical cavity such as sensitivity to

misalignment errors, mirror heating, and so on. Here we assume the commonly-used 1064 nm wavelength for the incident laser.

Taking these technical limitations into consideration, the electron bunches are preferably generated using a high repetition rate source with small emittance and energy spread. For a large flux a smaller electron beam spot size at the IP is needed; while a larger spot can be beneficial for a narrower scattered photon bandwidth, this ultimately depends on the ϵ_N/β^* ratio. However, it is preferable that an ICS source is capable of adjusting the optics at the IP to maximise the flux into a chosen bandwidth, as we describe later in Section IV C.

Previous consideration has been given by several groups as to the appropriate accelerator technology for intense ICS photon production, and here we summarise some key points. Linear accelerators (linacs) and ERLs share the benefit of being able to utilise small photoin-

jector emittances, and the Cornell injector has demonstrated normalised values < 1 mm-mrad for bunch charges up to at least 300 pC [20, 21]. Linacs are in practice limited to repetition rates < 10 kHz if using normal-conducting cavities, because of cavity heating limits. Superconducting linacs are limited perhaps to ~ 1MHz if energy recovery is not employed [22]; this is because un-recovered high-energy beam dump power eventually becomes intolerable [23, 24]. However, high-energy ERLs are now within reach due to the recent demonstration of multi-turn acceleration and recovery at CBETA, allowing for multi-milliampere operation.

When generating high energy photons, the operating power cost is significantly reduced with an ERL compared to a linac; a multi-turn ERL has the added benefit of requiring less floor space and fewer SRF cavities. Consequently, a multi-turn ERL with a high brightness, low energy spread electron beam at a high repetition rate is an ideal accelerator for an ICS source; CBETA is such an accelerator and we now discuss the anticipated operation of CBETA as an ICS source.

IV. INVERSE COMPTON PRODUCTION AT CBETA

A. Electron and Laser Beam Properties

Based on the desired properties of an electron beam given previously (high brightness, low energy spread) and the capabilities of CBETA [5], with the key design parameters given in Table I, the desired electron beam parameters at the IP are given in Table II. For each turn number, we have tabulated baseline parameters assuming the same β^* at the IP; below we show the optimised spot size and collimation angle required to maximise the flux into a 0.5% scattered photon bandwidth.

While the design of CBETA allows for a maximum current nearly eight times greater than the beam current assumed here, the coherent synchrotron radiation (CSR) disruption of the beam necessitates the lower bunch charge of 32 pC chosen [25]; the laser repetition rate cannot be increased due to the limitations of the optical cavity providing the laser repetition rate. As the focus of this paper is not on optical cavity design, laser parameters based on existing [16] and state-of-the-art systems [19] are assumed and are given in Table III.

During the single turn-commissioning of CBETA, the FFA was successfully tested with electron beams over an energy range from 39 to 59 MeV; we therefore consider that the ERL could be operated within this range to generate ICS photons. This would allow production of scattered photons with continuously-tuneable energy over the range 27.2 to 64.5 keV. Fig. 3 indicates the possible scattered photon energies using either the fixed energies of the 4 passes, or from the variable electron energy using a single pass. Since tuning of the scattered photon energy is likely to be done in practical ICS sources by varying
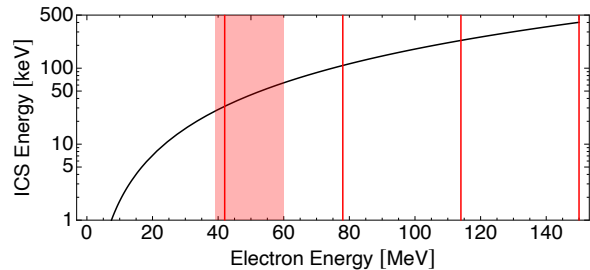

FIG. 3: An ICS source generating photons from each of the four CBETA ERL passes delivers the (fixed) scattered energies indicated here; we assume a fixed incident laser wavelength of 1064 nm. CBETA has also experimentally demonstrated tuning of single-pass acceleration from 39 to 59 MeV (indicated by the shaded region), which indicates the continuous tuning of scattered photon energy that an ERL in general might deliver.

the electron energy, this figure indicates the likely tuning range that is possible either at CBETA or (analogously) at higher-energy ERLs.

B. Interaction Bypass Lattice

To utilize CBETA as an inverse Compton scattering source, a bypass line is required that replaces the ordinary 4th pass due to the stringent space restrictions in the existing FFA system; this leaves no space to arrange IP focusing, nor for the laser re-circulation cavity. The scattered photons from the ICS must also be produced in a different plane to the existing accelerator; the photons must be safely extracted from the footprint of the ERL since there is no space for an experimental hutch within the existing CBETA hall. The layout of such a bypass line is shown in Fig. 4. The bypass is configured for 150 MeV 4th-pass operation but could be adapted to operate with all nominal energies. The bypass was designed and optimised using the BMAD accelerator simulation library [26] and the TAO program [27] for simulating high energy particle beams in accelerators.

The bypass line diverts the 150 MeV electron beam after the 4th linac pass in the corresponding S4 splitter line; the electron beam then re-enters the existing layout in the R4 line. The bypass replaces the FFA return loop, S4, from the 4th dipole onward and R4 up to the 4th dipole. The bypass will be located above the existing permanent magnet arc as the FFA arc is still used to transport the lower energy (42, 78, and 114 MeV) beams before and after the bypass.

A system of vertical doglegs, replacing sections of the S4 and R4 lines, are required to provide a 30 cm vertical elevation of the bypass line relative to the plane of the FFA return loop in order to avoid the existing accelerator. Bypass arc sections replace the existing FFA arc

TABLE II: Electron beam parameters envisaged at the CBETA ICS interaction point (IP). The given baseline parameters – which assume the same β^* at the IP – allow a comparison of flux and bandwidth at different energies. The optimised values beneath those are where we have maximised the flux into a 0.5% scattered photon bandwidth through a suitable combination of beam spot size and collimation angle.

| Parameter	Quantity				Unit
Turn number	1	2	3	4	
Electron kinetic energy, E_e	42	78	114	150	MeV
Repetition rate, f			162.5		MHz
Bunch charge, eN_e			32		pC
Transverse normalised rms emittance, ϵ_N			0.3		mm-mrad
rms bunch length, $\Delta\tau$			1.0 (3.33)		mm (ps)
Relative energy spread			5.0×10^{-4}		
		Baseline parameters			
β^* (at the IP)			1		cm
Electron bunch spot size, σ_{electron}	6.01	4.42	3.65	3.19	µm
		Optimised for 0.5% (narrow) bandwidth			
β^* (at the IP)	3.56	6.58	9.60	12.62	cm
Electron bunch spot size, σ_{electron}	11.34	11.34	11.34	11.34	µm
Collimation angle, θ_{col}	1.533	0.830	0.569	0.433	mrad
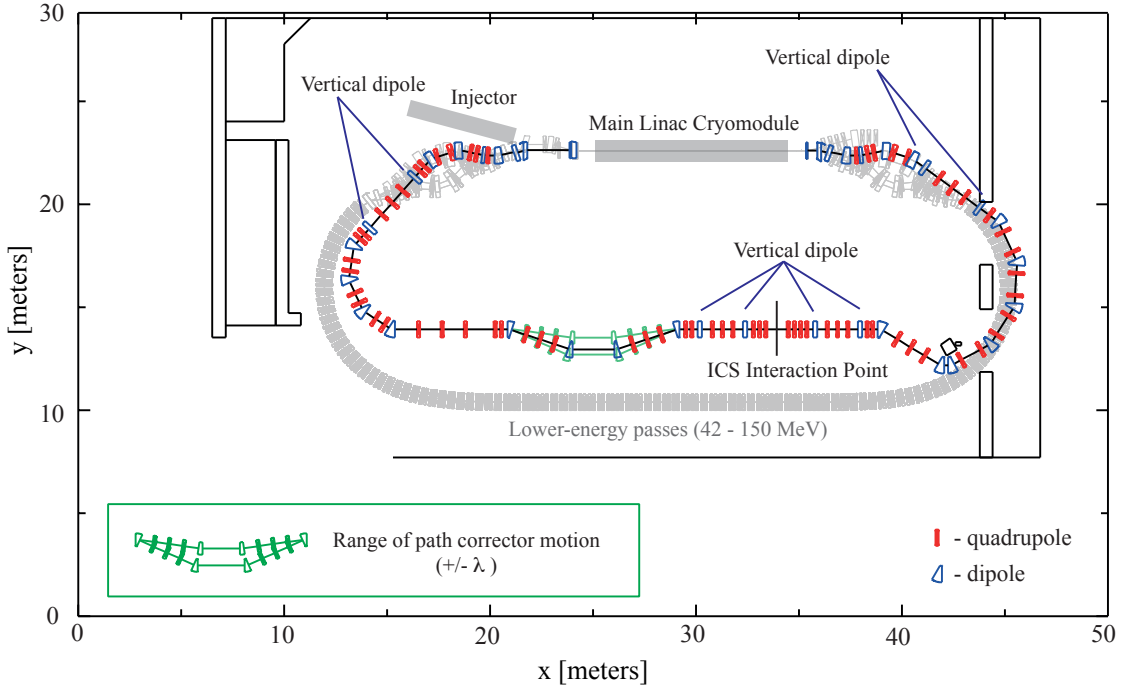
FIG. 4: Layout of the ICS bypass in CBETA; greyed beamline elements are already installed in the existing accelerator.

sections (FA, FB). Following the first arc, there is a horizontal dogleg used to close horizontal dispersion before the interaction region and offset the bypass from existing infrastructure.

At the interaction region (IR) the beam is again offset upward locally by a further 20 cm – to a 50 cm total offset above the FFA reference orbit height – using a pair of vertical doglegs; these are here called the IR doglegs.

The further vertical offset is imposed so the photons are produced in a different plane to both the bypass line and FFA return loop which is necessary for the extraction of the x-ray beam to an external experimental hutch and in order to avoid irradiation of the FFA permanent magnets. A flexible focusing section within the pair of IR doglegs is used to focus to the required beam waist. The final focus section is designed to enable both $\beta^* = 1$ cm for the

TABLE III: Laser pulse parameters at the IP.

Parameter	Quantity	Unit
Wavelength, λ_{laser}	1064	nm
Photon energy, E_{laser}	1.17	eV
Pulse energy	62	μJ
Number of photons, N_{laser}	3.3×10^{14}	
Repetition rate, f	162.5	MHz
Spot size at the IP, σ_{laser}	25	μm
Crossing angle, ϕ	5°	
Pulse length	10	ps
Relative energy spread, $\Delta E_{\text{laser}}/E_{\text{laser}}$	6.57×10^{-4}	

baseline case and $\beta^* = 12.6$ cm for the 0.5% bandwidth case (see Table II). The final focus section is constructed from 7 quadrupoles with the laser re-circulation cavity placed between the 4th and 5th quadrupole. This scheme allows the photons to be extracted via the first dipole of the downstream IR dogleg, minimizing the number of magnets requiring modification for photon extraction.

Within the straight section of the bypass following the IR, a variable path length adjustment is implemented based on the moving chicane described by by H. Owen et al [28]; this 4-dipole focusing chicane uses two mechanically-adjustable swing arms each incorporating a quadrupole triplet, and a central bellows. The chicane replicates the function of the S4/R4 splitter/recombiners to allow variation of both R_{56} and path length for re-entry into the MLC. Path length adjustment is made by opening the swing arms whilst increasing the dipole strengths accordingly; over a change in path length of $\pm\lambda_{RF}$ the variation in Twiss values (after re-matching) is moderate.

Optics tuning of the bypass is limited by the compact layout of CBETA, the conditions required for energy recovery of the interacted beam ($R_{56} = 0$), and the necessity for the bypass to be constructed above the existing FFA return loop; the β-functions and dispersion are however still feasible. Plots of β-functions and dispersion in the bypass line for the 0.5% bandwidth case are shown in Figs. 5 and 6.

C. Bandwidth Tuning

The bandwidth of the CBETA ICS is tuneable and can be selected on the basis of user requirements. Bandwidth selection is possible by tuning β^* at the IP and by setting the collimation angle, θ_{col} that collects the scattered photons; these may for example comprise switchable, fixed-aperture collimators.

Typically the dominant terms that define the bandwidth of an inverse Compton source (Eq. 16) are the collimation term (Eq. 17) and the emittance term (Eq. 20). The free parameter of the collimation term is the collimation angle θ_{col}, which can be adjusted either by changing the collimator aperture or changing its distance from
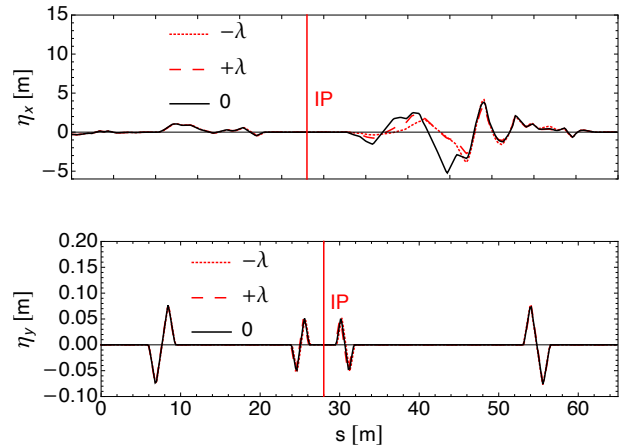

FIG. 5: Dispersion functions in the ICS bypass line for the 0.5% bandwidth case, showing the re-matched conditions for different path length configurations $-\lambda_{RF}$, 0 and $+\lambda_{RF}$. The ICS interaction point (IP) is indicated.
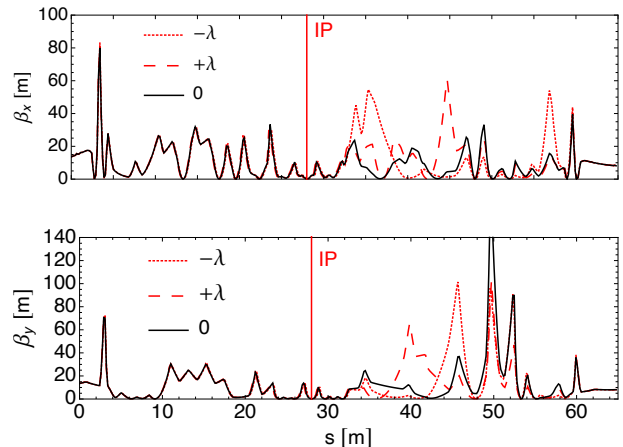

FIG. 6: Twiss functions in the ICS bypass line, showing the re-matched conditions for different path length configurations $-\lambda_{RF}$, 0 and $+\lambda_{RF}$. The ICS interaction point (IP) is indicated.

the IP. Adjustable collimators have been designed for the ELI-NP-GBS γ-ray ICS source [29]; a similar design could be implemented here.

The emittance term is dependent both on the normalised transverse emittance ϵ_N and on β^*. It is more convenient to change the β-function at the IP with focusing rather than by varying the emittance, since the latter is dependent on the injector and collective effects prior to the IP. By using a larger β^* and a small collimator aperture, it is possible to reduce the contribution of the collimation and emittance terms so that they are negligible; thus the beam energy spread term (Eq. 18) becomes dominant, assuming that the contribution of the laser energy spread term (Eq. 19) is small (which is typical in all

conventional lasers). This effectively places a lower limit on the bandwidth of an ICS source, i.e. it is limited by the energy spread of the electron beam $\Delta E_e / E_e$ as

$$\left(\frac{\Delta E_\gamma}{E_\gamma}\right)_{\min} \approx 2\frac{\Delta E_e}{E_e}. \qquad (21)$$

Consequently, any bandwidth above this limit can be achieved by an ICS source by tuning of the collimation angle and β^* so that a desired bandwidth, $\Delta E_\gamma / E_\gamma$, is achieved. Since the collimation and emittance terms are typically dominant, all other terms can be excluded and the solutions are bounded by

$$\frac{\Delta E_\gamma}{E_\gamma} > \sqrt{\left(\frac{\Delta\sigma_{\theta_{\text{col}}}}{E_{\theta_{\text{col}}}}\right)^2 + \left(\frac{\Delta\sigma_\epsilon}{E_\epsilon}\right)^2}. \qquad (22)$$

This results in myriad combinations of β^* and θ_{col} that satisfy a particular chosen bandwidth larger than this lower limit (Eq. 21).

The different β^*, θ_{col} combinations each give a different collimated flux; obviously we wish to chose the solution with the largest flux. The collimated flux $\mathcal{F}_\Psi$ of each solution is calculated based on a method valid for small collimation angles ($\gamma\theta_{\text{col}} < 1$) derived by C. Curatolo et al. [30]. Re-cast for our variable definitions, it becomes

$$\mathcal{F}_\Psi \propto \frac{\left(1 + \sqrt[3]{X}\Psi^2/3\right)\Psi^2}{[1 + (1 + X/2)\,\Psi^2]\,(1 + \Psi^2)}, \qquad (23)$$

where $\mathcal{F}$ is the total (uncollimated) flux, $\Psi = \gamma\theta_{\text{col}}$, and X is the recoil parameter. The solution giving the maximal flux is selected.

It is not practicable to calculate the flux from every combination of β^* and θ_{col}. Instead, an array of collimation angles θ_{col} from 0 to $1/\gamma$ is used ($\gamma\theta_{\text{col}} < 1$), and for a given bandwidth value the corresponding β^* is calculated using

$$\beta^* = \frac{2\gamma\epsilon_N}{\sqrt{\left(\frac{\Delta E_\gamma}{E_\gamma}\right)^2 - \left[\left(\frac{\sigma_{\theta_{\text{col}}}}{E_{\theta_{\text{col}}}}\right)^2 + \left(\frac{\sigma_e}{E_e}\right)^2 + \left(\frac{\sigma_{\text{laser}}}{E_{\text{laser}}}\right)^2\right]}}, \qquad (24)$$

which is a rearrangement of (Eq. 16). The solutions based on this array of collimation angles are shown in β^* - θ_{col} space in Fig. 7 for the case of 0 - 1% bandwidth for the CBETA ICS.

The collimated flux $\mathcal{F}_\Psi$ is calculated for each combination produced via this method. The maximal collimated flux is selected and the combination of β^* and θ_{col} corresponding to this solution is returned. This process can be applied to the case of a target bandwidth to determine θ_{col}, β^*, and collimated flux in the selected bandwidth. In addition, applying this method to a continuum of bandwidths allows us to map the possible operational settings of our ICS source, and to derive tuning curves such as the variation of the collimated flux with bandwidth (over a 0–1% bandwidth range), as shown in Fig. 8.
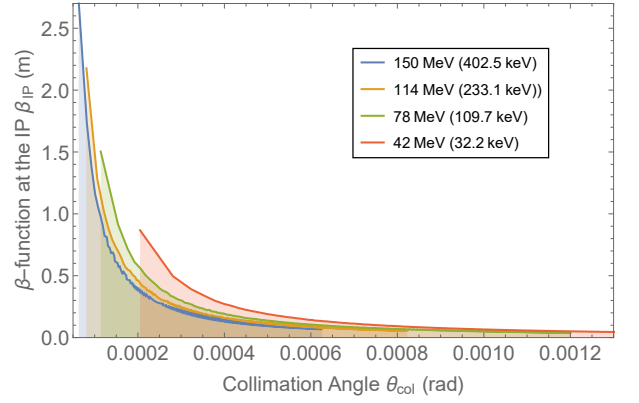

FIG. 7: Tuning curves of β^* against θ_{col} for each of the nominal CBETA electron beam energies satisfying the maximal flux across the 0–1% bandwidth range. Minimised bandwidth solutions in this range have large β-functions at the IP and small collimation angles θ_{col}; the maximal bandwidth solutions have small β-functions and larger collimation angles θ_{col}.
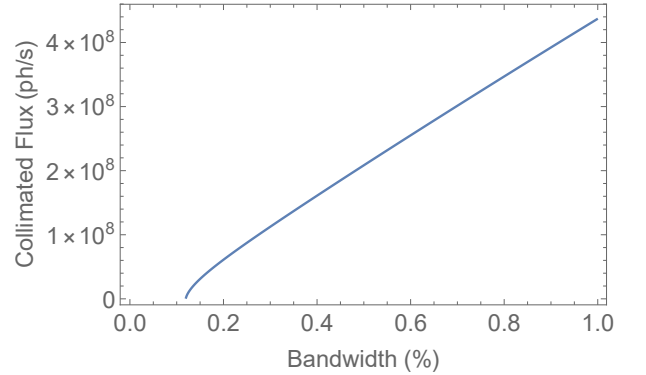

FIG. 8: Tuning curve of collimated flux against bandwidth for a 0–1% bandwidth range, produced by tuning β^* and θ_{col}. The tuning curve is independent of beam energy for scattering scenarios within the Thomson regime, hence this tuning curve applies to all energies in CBETA. The left end of tuning curve indicates the minimum possible bandwidth of the ICS source, which in CBETA is $\simeq 0.1\%$ and is determined by the electron beam energy spread.

D. X-ray Photon Production and Spectra

The predicted ICS production from CBETA has been calculated using the formulae derived in Section III A, and is shown in Table IV. This table shows the optimised collimated flux for 0.5% bandwidth which has been produced using the analytical method described in Section IV C. We see as expected that both the uncollimated and collimated fluxes are essentially independent of electron energy, which is typical of the ICS process. Using Eq. 7, we see that the uncollimated fluxes of Table IV vary by only around 2% due to the small effects of the

varying from 3 μm to 6 μm of the (unoptimised) beam sizes and of the varying σ_c. A larger effect is from the 5 degree crossing angle; this crossing angle only causes a small (c. 1 keV) reduction in the Compton edge energy of the spectrum, but it reduces the effective time over which the incident laser photons may interact with the electrons by about a factor of five.

The spectrum of the Compton-scattered photons has been calculated following the formalism of Sun et al. [11], which integrates the photons at each energy that pass through a given collimator aperture (here circular)[2]. Sun's method obtains the spectrum assuming a head-on geometry, and we validated our implementation against the results of this paper. We show the obtained CBETA spectral density for 150 MeV electrons in Fig. 9; this is scaled for the 32 pC/162.5 MHz CBETA bunch rate and to account for the 5 degree crossing angle. This integrated flux is consistent with the predicted collimated flux obtained using Curatolo's method (Eq. 23) that is shown in Table IV, and with Krafft's approximation $\mathcal{F}_{0.1\%} \simeq 1.5 \times 10^{-3} \dot{N}_\gamma$ [10].

Separately, we also obtained the predicted head-on flux using the code ICCS3D, a generalization of the ICCS code [12, 31, 32], which computes radiation produced in ICS operating in the linear Compton regime (when $a_0 \ll 1$, and electron recoil is properly accounted for). In ICCS3D, a 3D laser pulse model replaces the 1D plane wave model used in ICCS. This modification is implemented in a manner described in Terzic et al. [32]: instead of all electrons experiencing the same laser field strength a_0, as they do for a 1D plane wave, their effective laser field strength is dependent on the electron's distance from the laser's center at the moment of scattering. We compared ICCS3D using the parameters in Tables II and III; the obtained flux is consistent with the results obtained using Sun's and Curatolo's method. ICCS3D also allows a comparison between a Gaussian bunch and a realistic bunch that we tracked through the bypass lattice (obtained using BMAD as outlined in Section IV) using TAO. There is no significant difference in the obtained spectrum other than a < 1 keV shift in the peak scattered energy caused by a small (c. 0.1 MeV) asymmetry in the real electron energy distribution compared to an idealised Gaussian distribution. Since small variations in the actual operating energy of such a source are inevitable, we conclude that the Compton spectrum will not be significantly affected by the exact electron energy distribution in our situation.

---

[2] Note that there is an error in Equation 16 of Sun's paper, where the prefactor gives that $dN/dE \propto L^2$ for a source-to-collimator distance L. Clearly, this should be $dN/dE \propto 1/L^2$; the other parts of the given equation are correct
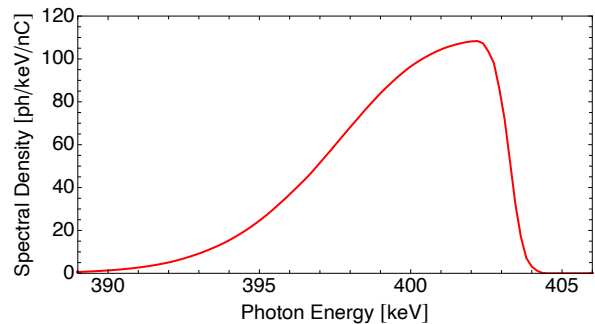

FIG. 9: Predicted spectral output (flux) from 1064 nm photons colliding head-on with the $E_e = 150$ MeV (kinetic energy) electrons in CBETA; this spectrum was generated using the ICCS3D code, and is consistent with calculations using the method of Sun et al. This spectrum has a peak energy of 403.3 keV; using the proposed 5 degree crossing angle, the peak energy is reduced to 402.5 keV and the spectral density is reduced by a factor ~ 5.

V. DISCUSSION

A. Comparison with Other Radiation Sources

Inverse Compton production of photons has the ability to extend the reach of monochromatic photon sources into the MeV range. Alternative sources are bremsstrahlung methods that generate intrinsically broad-spectrum radiation, line sources such as ^{137}Cs and ^{60}Co, and synchrotron radiation. Whilst line sources provide photons in the MeV scale, they are of course not tuneable, emit isotropically and are difficult to handle (they cannot be turned off). Synchrotron radiation sources such as undulators are presently the primary method to generate intense, tuneable radiation in the keV to MeV range.

The characteristic critical photon energy for SR is

$$\epsilon_c = \frac{3}{2} \frac{\hbar c \gamma^3}{\rho}, \tag{25}$$

which may be written as ϵ_c [keV] $\simeq 0.665 E^2 B$ (for E given in GeV and B in tesla); this sets the scale for attainable photon energy. The highest-energy 3rd-generation SR source today is SPRING-8 with $E = 8$ GeV and $B \simeq 0.68$ T to obtain a critical energy $\epsilon_c \simeq 29$ keV for its broadband incoherent SR production; it is unlikely that a storage ring above 8 GeV will be built since rings such as SPRING-8 already have a physical circumference exceeding 1000 m. The undulator output limit from a storage ring can be illustrated by setting the undulator K-parameter to be $K \sim 1$ and an undulator period $\lambda_u \sim 1$ cm. This gives a magnetic field limit of

$$B_0 = \frac{m_e c}{e} \frac{2\pi}{\lambda_u} K \sim 1\text{T}. \tag{26}$$

TABLE IV: Anticipated photon output for each of the four electron beam energies in CBETA, taking into account a 5 degree crossing angle. The uncollimated flux varies by around 2% due to the small effect of the electron spot size; $X < 0.003$ even at 150 MeV. The collimated flux has been optimised for a 0.5% bandwidth. The number of scattered photons is essentially independent of electron energy for a fixed electron spot size at the IP, and since both the Compton spectrum and the (relative) 0.5% bandwidth scale together with γ^2, both the optimised spot size and the predicted collimated fluxes are the same at all electron energies.

	Electron Kinetic Energy (MeV)				
	42	78	114	150	Unit
X-ray peak energy	32.2	109.7	233.1	402.5	keV
Uncollimated flux	3.16×10^{10}	3.20×10^{10}	3.21×10^{10}	3.22×10^{10}	ph/s
Spectral density	9.82×10^{5}	2.92×10^{5}	1.38×10^{5}	8.00×10^{4}	ph/s eV
Average brilliance	9.23×10^{10}	3.19×10^{11}	6.81×10^{11}	1.18×10^{12}	ph/s mm^2 mrad^2 0.1% bw
Peak brilliance	2.80×10^{15}	1.00×10^{16}	2.18×10^{16}	3.80×10^{16}	ph/s mm^2 mrad^2 0.1% bw
	0.5% bandwidth				
Collimated flux	2.09×10^{8}	2.09×10^{8}	2.09×10^{8}	2.09×10^{8}	ph/s 0.5% bw

The minimum undulator wavelength $K = 0$ possible (in the first harmonic of emission) is

$$\lambda_{\min} = \frac{\lambda}{2\gamma^2} \simeq 0.2\text{Å} \qquad (27)$$

at 8 GeV ($\gamma \simeq 15{,}700$), which corresponds to a photon energy of 60 keV. In practice, most hard x-ray undulators and wigglers operate up to around 100 keV photon energy, with very few existing beamlines extending beyond that. Undulator output at higher harmonics is limited predominantly by the presence of magnetic phase errors, and the reduction in ideal flux from an *rms* phase error σ_ϕ can be modelled approximately [33] using the factor

$$R = \exp(-n^2\sigma_\phi^2) \qquad (28)$$

where n is the (odd) undulator harmonic, and σ_ϕ has typical values of a few degrees [34]. In practice this limits undulators to typically $n < 15$ in operation, although there is some discussion of whether *rms* error may be pessimistic in some cases [35] and whether it may be reduced in future insertion devices [36, 37].

We have surveyed the hard x-ray sources presently available at the high-energy storage rings APS, ESRF-EBS, PETRA-III, and SPRING-8 [38–41], using the codes SPECTRA [42] and SRW [43] to validate expected spectral output [44]. An example is the SPRING-8 BL10XU beamline, whose flux including an *rms* phase error of 5 degrees is shown in Fig. 10; this is compared with tabulated sample fluxes at the source points presented by SPRING-8 [41] and with the predicted flux from the CBETA ICS source design here.

It was already pointed out by Krafft and Priebe [10] that the brilliance offered by ICS sources is not competitive at the photon energies provided for by synchrotron radiation facilities; here we predict brilliance values that are consistent with that conclusion. The predicted brilliance of CBETA at the four operating energies is compared in Fig. 11 with a high-energy undulator (BL10XU) at the world's highest-energy 3rd-generation synchrotron

source: SPRING-8 [41]. This undulator is indicative of what is achievable from other undulators on these high-energy sources. We see as expected that storage ring sources produce greater brilliance even at high harmonic number for photon energies up to at least 200 keV. However, the fundamental energy scaling of synchrotron radiation and the finite undulator magnetic field quality means that the ICS output from CBETA become superior in the 400 keV regime. This performance is mirrored in the predicted flux that is shown in Fig. 10, that makes the same assumption of a 5 degree *rms* phase error; the measured flux at 30 keV and 61 keV is superior to that possible from an ICS source, but at 400 keV this is reversed.

Fig. 12 compares the on-sample measured fluxes from those high-energy synchrotron beamlines (>30 keV) for which data is available [38–41]. Almost no beamline generates output above 100 keV, and above 400 keV we have shown that ICS is in any case a superior source. Extending the demonstrated CBETA parameters to higher electron energy we would expect the collimated flux values to remain nearly constant; hence we may estimate the likely possible flux for MeV-scale photons from an ERL-based source. Two indicative electron energies (300 MeV and 600 MeV) are also shown in Fig. 12.

B. Applications

The proposed CBETA ICS is a high-flux, small-bandwidth, quasi-monochromatic source of x-rays, producing high peak energy photons in the 100s keV range. The large flux opens up a parameter space for x-ray applications previously attainable only at the largest synchrotrons, and then only using substantial x-ray optics. We now outline some possible uses.

Important applications of such a source are x-ray absorption spectroscopy and x-ray fluorescence [45]. High-energy XRF is an application that is particularly well-suited for this ICS source; due to collimation there is no
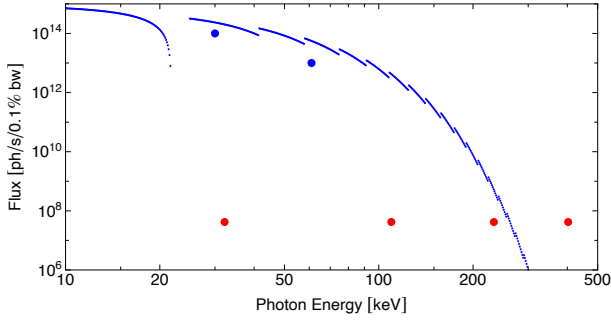
FIG. 10: Comparison of CBETA predicted flux (here flux in a 0.1% bandwidth to allow comparison with conventional calculations of undulator flux) at the four discrete operating energies given in Table IV with the output from a typical high-energy undulator. The undulator shown is the SPRING-8 BL10XU insertion device [41] assuming an *rms* phase error of 5 degrees. Whilst this undulator is not designed to deliver good output at high harmonic number, it offers a useful guide to possible 3rd-generation source output in the 100 keV to 500 keV range. the measured flux at 30 keV and 61 keV for this beamline is also shown [41]. We predict that CBETA flux at 402 keV (150 MeV electron energy) exceeds that from 3rd-generation sources.
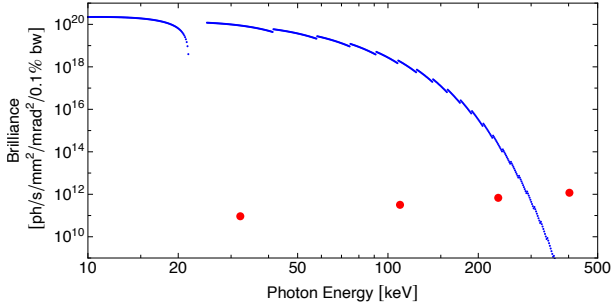

FIG. 11: Comparison of CBETA predicted brilliance at the four discrete operating energies given in Table IV with the output from a typical high-energy undulator. The undulator shown is the SPRING-8 BL10XU insertion device [41] assuming an *rms* phase error of 5 degrees. We predict that CBETA brilliance at 402 keV (150 MeV electron kinetic energy) exceeds that from 3rd-generation sources.

need to monochromate, avoiding complex x-ray optical instrumentation. Energy-sensitive x-ray fluorescence detection can be provided by a solid-state detector coupled to a pulse-height analyzer. For example, in any analysis of a fission reactor's fuel rods, the $K\alpha$ and $K\beta$ lines for uranium ($K\alpha_1 = 98.4$ keV, $K\beta_1 = 111.3$ keV) and plutonium ($K\alpha_1 = 103.7$ keV, $K\beta_1 = 117.2$ keV) could be probed [46]. Quantitative assays would be performed by means of a low-Z reference scatterer to ascertain the spectral content of the broadband incident beam through elastic and Compton scattering into the same detector.
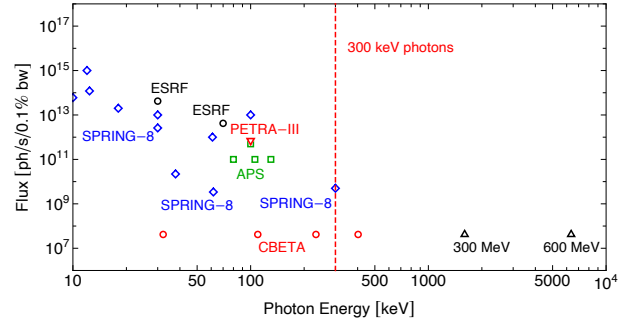

FIG. 12: On-sample measured fluxes from APS, ESRF-EBS, PETRA-III, and SPRING-8 for which information has been published [38–41]. This is compared with the predicted CBETA outputs at the 4 discrete photon energies from 32 to 402 keV, and the predicted flux obtained by scaling the CBETA electron energy to 300 MeV (1600 keV photons) and 600 MeV (6360 keV photons). Whilst 3rd-generation sources are superior to ICS sources up to photon energies around 300 keV, they do not produce useable flux above 400 keV.

The fluorescence efficiency of the detection scheme is then provided by the known photo-absorption cross sections of the elements of interest versus incident energy.

The deep penetrating power of a high-energy x-ray source provides the opportunity for imaging of thick specimens that would would not be possible at lower energies. These range from straightforward techniques such as 2D shadowgraphy through to 3D reconstruction with tomography [47].

Another ready application exploits the high flux and high energy of the source: energy-dispersive x-ray diffraction (EDXRD) for the identification of constituents of a polycrystalline/powdered sample. A high-flux source would allow for rapid identification of the minerals in a mined ore sample, while the high energy of the source allows for the inspection of thick specimens. In EDXRD [48] one applies the non-monochromated peak to a specimen of the material of interest, and checks for diffracted photons with an energy-sensitive solid-state detector. From the energy we deduce the wavelength, and applying the Bragg relation we find the combination of Miller indices and lattice spacing of the reflecting crystalline planes. Checking for many such reflections in a particular mineral provides constituent identification; the intensity of these Bragg peaks provides the relative abundances of the various mineral components. Our source serves as a high flux alternative to SR facilities [49] which typically operate up to 200 keV. Additionally, our design provides photons well beyond that energy range.

Turning to more ambitious but equally exciting applications, significant beamline infrastructure would be required here in contrast to the applications just discussed. In the first, we propose to perform non-resonant inelastic x-ray scattering (NIXS) in order to examine the dynamic

electronic response of quantum materials throughout the periodic chart. The high incident photon energy and large flux provided by our source allows us to test exciting materials such as transition metal oxides, which are a testbed for theories such as the Mott-Hubbard model, since they provide fresh insight into the candidates for useful applications such as high-temperature superconductors [50, 51]. The energy resolution requirements for this method are severe: 1 eV out of 100 keV; it would require the development of high-energy x-ray monochromator and analyzer optics, most likely through synthetic multi-layers in order to provide an optimal match to beam optics. In our implementation of the NIXS technique the analyzers are arrayed at a range of scattering angles to provide a comprehensive set of momentum transfers. The pass energy of the analyzers is fixed while the incident energy is scanned to provide variable energy transfers with a double crystal monochromator configuration [52, 53]. Because of sample self absorption and the weak signal set by the small Thomson cross section [52], the reach of NIXS is especially limited for medium to large Z elements. Performance of NIXS at an incident energy of 100 keV as proposed here would provide an attenuation length due to photoabsorption of 100 microns [54]. This is a factor of 25 greater [55] than that provided at the contemporary hard NIXS facility at the Advanced Photon Source [53] which operates with an incident energy of 10 keV when performing spectroscopy at the low energy transfers of great interest in condensed matter studies.

In our second ambitious application of Compton-produced photons, a mixing crystal would be employed to generate entangled photon pairs via parametric down conversion (PDC). Here the efficiency is boosted by working at high input photon energy, since the intensity of the vacuum fluctuations present at the mixer's input varies as the fourth power of the operating energy [56]. Besides the accomplishment of achieving PDC at (about) a factor of five higher energy than is currently practised [57], it will provide exciting applications, for example twin microscopy – which promises enhanced visibility through quantum ghost imaging of otherwise inaccessible specimens – and twin ellipsometry for the careful examination of surface structures [58]. To compare PDC applications with contemporary SR sources: the ghost imaging demonstration of Schori et al. [57] was recently performed with an input energy of 22.3 keV. Using our source at 100 keV would provide PDC generation according to the aforementioned scaling law with a zero point energy flux advantage of about 400 greater.

The final ambitious application, nuclear resonance fluorescence (NRF), is a technique suitable for a future, higher-energy ERL-based ICS, with an electron beam energy on the order of 350 MeV or above. This electron beam energy regime boosts the Compton back scattered photons into the regime of gamma rays with an energy of 2.2 MeV or above. These in turn would be used to excite nuclear levels identifying them with a energy

sensitive solid state detector, achieving the nuclear sister spectroscopy to the atomic fluorescence spectroscopy mentioned in our first application. Such spectroscopy would be very useful in assaying nuclear materials, for example identification of manufacturing defects in fission fuel assemblies, nonproliferation security of spent fission fuel and identification of unknown legacy wastes [59–63]. Moving up to photon energies above 5 MeV (requiring a GeV-scale electron ERL) would open up the nuclear transmutation reactions (γ, p), (γ, n), (γ, f) with potentially far-reaching applications in waste transmutation [64], the understanding of fission dynamics [65–67] and bespoke medical isotope production from existing waste streams [68].

VI. CONCLUSION

In this paper we have shown a method of adapting an existing multi-turn energy-recovery linac to produce a quasi-monochromatic source of photons in the 100s keV range with higher flux and spectral density than hitherto achieved. We establish that such a source is highly desired for a range of scientific and industrial applications that are not yet fully served by existing sources. A specific design of electron transport beamline for the CBETA energy recovery linac is presented which is compatible with the existing accelerator. This additional beamline enables an inverse Compton scattering interaction with a Fabry-Perot laser cavity. The expected output properties are derived and compared to monochromated photons of the same energy generated by much larger storage-ring-based facilities, thereby demonstrating the competitiveness of this approach.

ACKNOWLEDGMENTS

[1] R. Hajima *et al.*, Application of laser compton scattered gamma-ray beams to nondestructive detection and assay of nuclear material, The European Physical Journal Special Topics **223**, 1229 (2014).

[2] A. Bartnik, N. Banerjee, D. Burke, J. Crittenden, K. Deitrick, J. Dobbins, C. Gulliford, G. H. Hoffstaetter, Y. Li, W. Lou, P. Quigley, D. Sagan, K. Smolenski, J. S. Berg, S. Brooks, R. Hulsart, G. Mahler, F. Meot, R. Michnoff, S. Peggs, T. Roser, D. Trbojevic, N. Tsoupas, and T. Miyajima, CBETA: First Multipass Superconducting Linear Accelerator with Energy Recovery, Phys. Rev. Lett. **125**, 044803 (2020).

[3] G. Hoffstaetter, V. Litvinenko, and H. L. Owen, Nucl. Inst. Meth. **A557**, 345 (2006).

[4] L. Merminga, D. R. Douglas, and G. A. Krafft, High-current energy-recovering electron linacs, Annual Review of Nuclear and Particle Science **53**, 387 (2003), https://doi.org/10.1146/annurev.nucl.53.041002.110456.

[5] G. Hoffstaetter, D. Trbojevic, and C. Mayes, *CBETA design report*, Tech. Rep. (Brookhaven National Laboratory (BNL), Upton, NY (United States), 2017).

[6] E. Feenbergand H. Primakoff, Interaction of cosmic-ray primaries with sunlight and starlight, Phys. Rev. **73**, 449 (1948).

[7] R. H. Milburn, Electron scattering by an intense polarized photon field, Phys. Rev. Lett. **10**, 75 (1963).

[8] F. Arutyunianand V. Tumanian, The compton effect on relativistic electrons and the possibility of obtaining high energy beams, Physics Letters **4**, 176 (1963).

[9] C. Bemporad, R. H. Milburn, N. Tanaka, and M. Fotino, High-energy photons from compton scattering of light on 6.0-gev electrons, Phys. Rev. **138**, B1546 (1965).

[10] G. A. Krafftand G. Priebe, Compton sources of electromagnetic radiation, Reviews of Accelerator Science and Technology **03**, 147 (2010), https://doi.org/10.1142/S1793626810000440.

[11] C. Sun, J. Li, G. Rusev, A. Tonchev, and Y. Wu, Energy and energy spread measurements of an electron beam by compton scattering method, Physical Review Special Topics-Accelerators and Beams **12**, 062801 (2009).

[12] N. Ranjan, B. Terzić, G. Krafft, V. Petrillo, I. Drebot, and L. Serafini, Simulation of inverse compton scattering and its implications on the scattered linewidth, Physical Review Accelerators and Beams **21**, 030701 (2018).

[13] H. R. Weller, M. W. Ahmed, H. Gao, W. Tornow, Y. K. Wu, M. Gai, and R. Miskimen, Research opportunities at the upgraded hiγs facility, Progress in Particle and Nuclear Physics **62**, 257 (2009).

[14] T. Suzuki, *General formulae of luminosity for various types of colliding beam machines*, Tech. Rep. (National Lab. for High Energy Physics, 1976).

[15] V. B. Berestetskii, L. E. M., and P. L. P., *Quantum Electrodynamics*, Vol. 4 (Pergamon, 1982).

[16] T. Akagi, A. Kosuge, S. Araki, R. Hajima, Y. Honda, T. Miyajima, M. Mori, R. Nagai, N. Nakamura, M. Shimada, T. Shizuma, N. Terunuma, and J. Urakawa, Narrow-band photon beam via laser compton scattering in an energy recovery linac, Phys. Rev. Accel. Beams **19**, 114701 (2016).

[17] K. E. Deitrick, G. A. Krafft, B. Terzić, and J. R. Delayen, High-brilliance, high-flux compact inverse compton light source, Phys. Rev. Accel. Beams **21**, 080703 (2018).

[18] F. Hartemann, W. Brown, D. Gibson, S. Anderson, A. Tremaine, P. Springer, A. J. Wootton, E. Hartouni, and C. Barty, High-energy scaling of compton scattering light sources, Physical Review Special Topics-Accelerators and Beams **8**, 100702 (2005).

[19] H. Carstens, N. Lilienfein, S. Holzberger, C. Jocher, T. Eidam, J. Limpert, A. Tünnermann, J. Weitenberg, D. C. Yost, A. Alghamdi, *et al.*, Megawatt-scale average-power ultrashort pulses in an enhancement cavity, Optics letters **39**, 2595 (2014).

[20] C. Gulliford, A. Bartnik, I. Bazarov, L. Cultrera, J. Dobbins, B. Dunham, F. Gonzalez, S. Karkare, H. Lee, H. Li, Y. Li, X. Liu, J. Maxson, C. Nguyen, K. Smolenski, and Z. Zhao, Demonstration of low emittance in the cornell energy recovery linac injector prototype, Phys. Rev. ST Accel. Beams **16**, 073401 (2013).

[21] A. Bartnik, C. Gulliford, I. Bazarov, L. Cultera, and B. Dunham, Operational experience with nanocoulomb bunch charges in the cornell photoinjector, Phys. Rev. ST Accel. Beams **18**, 083401 (2015).

[22] J. Stohr, Linac coherent light source ii (lcls-ii) conceptual design report 10.2172/1029479.

[23] S. M. Gruner, D. Bilderback, I. Bazarov, K. Finkelstein, G. Krafft, L. Merminga, H. Padamsee, Q. Shen, C. Sinclair, and M. Tigner, Energy recovery linacs as synchrotron radiation sources (invited), Review of Scientific Instruments **73**, 1402 (2002), https://doi.org/10.1063/1.1420754.

[24] L. Merminga, D. R. Douglas, and G. A. Krafft, High-current energy-recovering electron linacs, Annual Review of Nuclear and Particle Science **53**, 387 (2003), https://doi.org/10.1146/annurev.nucl.53.041002.110456.

[25] W. Louand G. H. Hoffstaetter, Coherent synchrotron radiation wake expressions with two bending magnets and simulation results for a multiturn energy-recovery linac, Phys. Rev. Accel. Beams **23**, 054404 (2020).

[26] D. Sagan, The Bmad Manual, Available at: `https://www.classe.cornell.edu/bmad/manual.html` ((2019)).

[27] D. Sagan, The Tao Manual, Available at: `https://www.classe.cornell.edu/bmad/tao.html` ((2019)).

[28] H. L. Owenand P. H. Williams, A modular path length corrector for recirculating linacs, Nuclear Instruments and Methods in Physics Research Section A: Accelerators, Spectrometers, Detectors and Associated Equipment **662**, 12 (2012).

[29] G. Paternò, P. Cardarelli, M. Marziani, E. Bagli, F. Evangelisti, M. Andreotti, M. Gambaccini, V. Petrillo, I. Drebot, A. Bacci, *et al.*, A collimation system for eli-np gamma beam system–design and simulation of performance, Nuclear Instruments and Methods in Physics Research Section B: Beam Interactions with Materials and Atoms **402**, 349 (2017).

[30] C. Curatolo, I. Drebot, V. Petrillo, and L. Serafini, Analytical description of photon beam phase spaces in inverse compton scattering sources, Phys. Rev. Accel. Beams **20**, 080701 (2017).

[31] G. Krafft, E. Johnson, K. Deitrick, B. Terzić, R. Kelmar, T. Hodges, W. Melnitchouk, and J. Delayen, Laser pulsing in linear compton scattering, Physical Review Accelerators and Beams **19**, 121302 (2016).

[32] B. Terzić, A. Brown, I. Drebot, T. Hagerman, E. Johnson, G. A. Krafft, C. Maroli, V. Petrillo, and M. Ruijter, Improving performance of inverse compton sources through laser chirping, EPL (Europhysics Letters) **126**, 12003 (2019).

[33] R. Walker, Interference effects in undulator and wiggler radiation sources, Nuclear Instruments and Methods in Physics Research Section A: Accelerators, Spectrometers, Detectors and Associated Equipment **335**, 328 (1993).

[34] R. P. Walker, Phase errors and their effect on undulator radiation properties, Phys. Rev. ST Accel. Beams **16**, 010704 (2013).

[35] T. Tanaka, Universal representation of undulator phase errors, Phys. Rev. Accel. Beams **21**, 110704 (2018).

[36] C. S. Hwang, J. C. Jan, C. S. Chang, S. D. Chen, C. H. Chang, and T. M. Uen, Development trends for insertion devices of future synchrotron light sources, Phys. Rev. ST Accel. Beams **14**, 044801 (2011).

[37] J.-C. Huang, H. Kitamura, C.-K. Yang, C.-H. Chang, C.-H. Chang, and C.-S. Hwang, Challenges of in-vacuum and cryogenic permanent magnet undulator technologies, Phys. Rev. Accel. Beams **20**, 064801 (2017).

[38] APS beamline list, `https://www.aps.anl.gov/Beamlines/Directory`, accessed: 2020-08-28.

[39] ESRF-EBS beamline list, `https://www.esrf.eu/home/UsersAndScience/Accelerators/ebs---extremely-brilliant-source/ebs-parameters.html`, accessed: 2020-08-28.

[40] PETRA III beamline list, `https://photon-science.desy.de/facilities/petra_iii/beamlines/index_eng.html`, accessed: 2020-08-28.

[41] SPRING-8 beamline list, `http://www.spring8.or.jp/en/about_us/whats_sp8/facilities/bl/list/`, accessed: 2020-08-28.

[42] T. Tanaka and H. Kitamura, *SPECTRA*: a synchrotron radiation calculation code, Journal of Synchrotron Radiation **8**, 1221 (2001).

[43] O. Chubar, A. Fluerasu, L. Berman, K. Kaznatcheev, and L. Wiegart, Wavefront propagation simulations for beamlines and experiments with "synchrotron radiation workshop", Journal of Physics: Conference Series **425**, 162001 (2013).

[44] T. Tanaka, T. Seike, X. Maréchal, T. Bizen, T. Hara, and H. Kitamura, Field measurement and correction of the very long in-vacuum x-ray undulator at the spring-8, Nuclear Instruments and Methods in Physics Research Section A: Accelerators, Spectrometers, Detectors and Associated Equipment **467-468**, 149 (2001), 7th Int.Conf. on Synchrotron Radiation Instrumentation.

[45] P. Willmott, *An introduction to synchrotron radiation: techniques and applications* (John Wiley & Sons, 2019) Chap. Spectroscopic Techniques.

[46] G. J. Havrilla, V. Lopez, K. McIntosh, W. Elam, and D. Robinson, Feasibility of uranium detection through container walls using ultrahigh-energy x-ray fluorescence, Microscopy Today **23**, 30 (2015).

[47] J. Als-Nielsen and D. McMorrow, *Elements of Modern X-Ray Physics* (Wiley, 2011) Chap. 9.

[48] B. Kämpfe, F. Luczak, and B. Michel, Energy dispersive x-ray diffraction, Particle & Particle Systems Characterization **22**, 391 (2005).

[49] Structural materials beamline, `https://www.chess.cornell.edu/structural-materials-beamline`, accessed: 2020-08-13.

[50] M. Hasan, P. Montano, E. Isaacs, Z.-X. Shen, H. Eisaki, S. Sinha, Z. Islam, N. Motoyama, and S. Uchida, Momentum-resolved charge excitations in a prototype one-dimensional mott insulator, Physical review letters **88**, 177403 (2002).

[51] E. Isaacs and P. Platzman, Inelastic x-ray scattering in condensed matter physics, Physics Today **Feb.**, 40 (1996).

[52] W. Schülke, *Electron dynamics by inelastic X-ray scattering*, Chapters 2 and 3 (Oxford University Press, 2007).

[53] T. Fister, G. Seidler, L. Wharton, A. Battle, T. Ellis, J. Cross, A. Macrander, W. Elam, T. Tyson, and Q. Qian, Multielement spectrometer for efficient measurement of the momentum transfer dependence of inelastic x-ray scattering, Review of scientific instruments **77**, 063901 (2006).

[54] Transmitted intensity and linear attenuation coefficient, `https://www.nde-ed.org/EducationResources/CommunityCollege/Radiography/Physics/attenuationCoef.htm`, accessed: 2020-08-13.

[55] Tungsten, `https://physics.nist.gov/PhysRefData/XrayMassCoef/ElemTab/z74.html`, accessed: 2020-08-13.

[56] P. Eisenberger and S. McCall, X-ray parametric conversion, Physical Review Letters **26**, 684 (1971).

[57] A. Schori, D. Borodin, K. Tamasaku, and S. Shwartz, Ghost imaging with paired x-ray photons, Physical Review A **97**, 063804 (2018).

[58] D. S. Simon, G. Jaeger, and A. V. Sergienko, *Quantum Metrology, Imaging, and Communication* (Springer, 2017) Chap. 4 and 7.

[59] D. Angal-Kalinin *et al.*, PERLE. powerful energy recovery linac for experiments. conceptual design report, Journal of Physics G: Nuclear and Particle Physics **45**, 065003 (2018).

[60] C. Angell, R. Hajima, T. Hayakawa, T. Shizuma, H. Karwowski, and J. Silano, Demonstration of a transmission nuclear resonance fluorescence measurement for a realistic radioactive waste canister scenario, Nuclear Instruments and Methods in Physics Research Section B: Beam Interactions with Materials and Atoms **347**, 11 (2015).

[61] A. M. Bolind and M. Seya, The State of the Art of the Nondestructive Assay of Spent Nuclear Fuel Assemblies - A Critical Review of the Spent Fuel NDA Project of the U . S . Department of Energy ' s Next Generation Safeguards Initiative - 10.11484/jaea-review-2015-027 (2015).

[62] C. Geddes, B. Ludewigt, J. Valentine, B. Quiter, M.-A. Descalle, G. Warren, M. Kinlaw, S. Thompson, D. Chichester, C. Miller, and S. Pozzi, Impact of Monoenergetic Photon Sources on Nonproliferation Applications, Osti 1376659, Inl/Ext–17-41137 (2017).

[63] E. Kwan, G. Rusev, A. S. Adekola, F. Dönau, S. L. Hammond, C. R. Howell, H. J. Karwowski, J. H. Kelley, R. S. Pedroni, R. Raut, A. P. Tonchev, and W. Tornow, Discrete deexcitations in U-235 below 3 MeV from nuclear resonance fluorescence, Physical Review C **83**, 041601 (2011).

[64] H. u. Rehman, J. Lee, and Y. Kim, Optimization of the laser-Compton scattering spectrum for the transmutation of high-toxicity and long-living nuclear waste, Annals of Nuclear Energy **105**, 150 (2017).

[65] G. Bellia, A. Zoppo, C. Maiolino, E. Migneco, and G. Russo, Towards a better understanding of deep subthreshold photofission of238U, Zeitschrift fr Physik A Atoms and Nuclei **314**, 43 (1983).

[66] M. Bhike, W. Tornow, Krishichayan, and A. P. Tonchev, Exploratory study of fission product yield determination from photofission of Pu 239 at 11 MeV with monoenergetic photons, Physical Review C **95**, 024608 (2017).

[67] Krishichayan, S. W. Finch, C. R. Howell, A. P. Tonchev, and W. Tornow, Monoenergetic photon-induced fission cross-section ratio measurements for U 235 , U 238 , and Pu 239 from 9.0 to 17.0 MeV, Physical Review C **98**, 014608 (2018).

[68] D. Habsand U. Köster, Production of medical radioisotopes with high specific activity in photonuclear reactions with γ-beams of high intensity and large brilliance, Applied Physics B: Lasers and Optics **103**, 501 (2011).